1 *Article*

2 # Geochronology and Geochemistry of Archean
3 # TTG and Tremolite Schist Xenoliths in Yemadong
4 # Complex: Evidence for ≥3.0Ga Archean
5 # Continental Crust in Kongling High-grade
6 # Metamorphic Terrane, Yangtze Craton, China

7 **Yunxu Wei[1,2,3], Wenxiao Zhou[4*], Zhengxiang Hu[5], Xianxiao Huang[4,6], Haiquan Li[4] and**
8 **Xiaoming Zhao[1,2,3]**

9 [1] Wuhan Center of China Geological Survey, Wuhan 430205, China
10 [2] Central South China Innovation Center for Geosciences，Wuhan 430205, China
11 [3]   Research Center of Granitic Diagenesis and Mineralization, China Geological Survey, Wuhan 430205, China
12 [4] Institute of geological survey, China University of Geosciences, Wuhan 430074, China
13 [5] Hubei Geological Survey, Wuhan, 430205, China
14 [6] Guangxi Regional Geological Survey, Guilin, 541001, China
15 ***** Correspondence: zhouwenxiao@cug.edu.cn; Tel.: +86 18607142327

17 **Abstract:** The origin and significance of the tonalite–trondhjemite–granodiorite (TTG) units
18 and the familiar metabasite xenoliths they host in the Yangtze Craton, China, remain
19 controversial, and resolving these issues is important if we are to understand the evolution of
20 the early Yangtze Craton. We focused on biotite–tremolite schist xenoliths in the Archean TTG
21 units of the Kongling high-grade metamorphic terrane, and U–Pb dating of their zircons
22 yielded $^{207}Pb/^{206}Pb$ ages of ca. 3.00 Ga, which provides a minimum age for the formation of the
23 pre-metamorphic basic igneous rock. The host TTGs and late intrusive granitic dikes yield
24 three groups of upper intercept ages at 2.87–2.88, 2.91–2.94, and 3.07 Ga, and a concordant age
25 at 2.94 Ga, which suggest that the Yangtze continental nucleus underwent three important
26 metamorphic–magmatic events in the Mesoarchean at ca. 3.00, 2.94, and 2.87 Ga. The biotite–
27 tremolite schists have high ratios of K_2O/Na_2O and high contents of CaO, Cr, and Ni, thus
28 showing the characteristics of high-K calc-alkaline island-arc volcanic rocks (basalt–andesite)
29 that form by the partial melting of subducted oceanic crust. The data also provide further
30 proof that a Mesoarchean metamorphic basement exists in the Yangtze Plate. Derivation of
31 the magmatic protoliths of the biotite–tremolite schist enclaves from an oceanic crust during
32 slab subduction, and the presence of these xenoliths within the TTG suite, indicate the
33 existence of the initiation of plate tectonics during the Mesoarchean (≤2.94 Ga)..

34 **Keywords:** Archean TTG; Tremolite Schist; Yemadong Complex; Kongling High-grade
35 Metamorphic Terrane; Yangtze Craton

36

1. Introduction

38   The two largest cratons in China, the South China Block (SCB) and the North China Craton
39 (NCC), collided along the Qinling–Dabie–Sulu orogenic belt in the Triassic or earlier [1, 2].
40 However, Archean rocks are relatively scarce in the SCB [3] compared with the NCC where
41 they are widely present [4-6]. The Kongling high-grade metamorphic terrane (KHMT) is the
42 nucleus of the Yangtze Block, and one of just a few Archean terranes reported so far in the SCB
43 [7-11]. Various ages for these rocks have been obtained during previous geochronological

44 studies, especially for the TTG gneisses in the KHMT [7-10, 12], but it is generally accepted that
45 the peak period of TTG magmatism occurred at 2.90–2.85 Ga, and magmatic rocks older than
46 3.0 Ga are relatively rare [7, 9, 13, 14]. Previous studies of these Archean crustal rocks in the
47 SCB have been limited, producing just a few isolated geochemical or geochronological data [7-
48 9, 11, 13, 15-17]. Outcrops of Neoarchean and Mesoarchean rocks have not been directly
49 identified in the field in the Yangtze Craton, and whether or not even more ancient rocks exist
50 in the Yangtze Craton is a problem yet to be solved. In the absence of clear evidence from rocks
51 in the field, the main stages of formation of the KHMT have been unclear, and this also means
52 that issues about the early formation and evolution of the nucleus of the Yangtze Craton have
53 remained controversial.

54 **2. Geological background and sample descriptions**

55 *2.1. Geological background*

56   The SCB was formed by the Grenvillian continental collision [18] of the Yangtze Craton
57 and the Cathaysia Block. The Yangtze Craton is bounded to the west by the Songpan–Ganzi
58 Block, to the north by the Qinling–Dabie–Sulu Orogen, and to the south by the Jiangnan Orogen
59 (Figure 1a). The Kongling Terrane is in the northeastern part of the Yangtze Craton, has an oval
60 dome structure, and covers an area of ~360 km² (Figure 1b). It is divided by the Wuduhe Fault
61 into two segments known as the North Kongling Terrane, dominated by Archean TTG granitic
62 gneisses and metasedimentary rocks (Figure 1c)[7, 19], and the South Kongling Terrane,
63 dominated by Neoproterozoic TTG intrusions such as the Huangling Dome [20-22]. Previous
64 studies have revealed three major episodes of Archean crustal growth in the Kongling Terrane
65 at 3.3–3.2, 2.9–2.8, and 2.7–2.6 Ga [7-9, 15, 19, 23]. The 3.3–3.2 Ga TTG gneisses and migmatites
66 are preserved locally in the widespread 2.9–2.8 Ga TTG rocks [7, 8, 19, 23], and the 2.7–2.6 Ga
67 A-type granitic gneisses, discovered recently in the eastern North Kongling Terrane, mark the
68 termination of the subduction-related TTG magmatism and the addition of significant juvenile
69 crustal components [15]. Crustal materials as old as 3.8 Ga have only been inferred from zircon
70 Hf model ages [7, 8], and although one 3.8 Ga detrital zircon has been reported in the Kongling
71 Terrane from a Neoproterozoic sandstone [10], its source is uncertain.

72
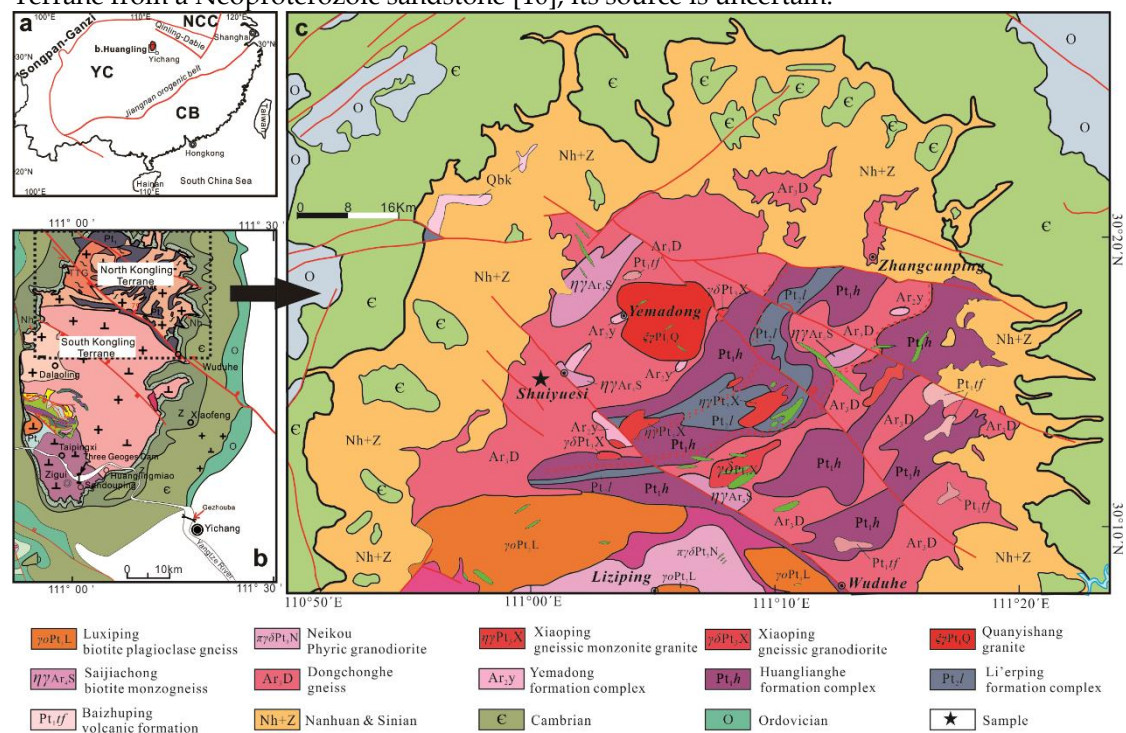
73   **Figure 1.** Geological map of the Archean Kongling Terrane (modified from Gao et al., 2011). (a)
74   Major tectonic divisions of South China. NCC denotes the North China Craton, YC denotes the
75   Yangtze Craton, and CB denotes the Cathaysia Block. (b) Structure and division of the
76   Kongling Terrane. (c) Geological map of the North Kongling Terrane. Star denotes the sample
77   location.

78   *2.2. Sampling*

79   Samples D0002-1 (biotite–tremolite schist), D0002-2 (tonalitic gneiss), D0002-3
80   (trondhjemitic gneiss), D0002-5 (granitic gneiss), and KH110 (granitic gneiss) are fresh rock
81   samples that were taken from a fracture surface (Figure 2a) near the Xiafangxi River (31°08′25″
82   N, 111°00′04″ E) in the North Kongling Terrane, and we also collected one sample of fresh
83   granitic gneiss (D0002-4) from Shuiyuesi village (on the other side of the river at 31°08′24″ N,
84   111°00′05″ E) (Figure 1c). Samples SMK-1 (trondhjemitic gneiss) and SMK-4 (trondhjemitic
85   gneiss) were collected from Shimenkou to the northwest of Wuduhe town near a streamlet
86   (31°10′11″N, 111°11′22″E). The exposed lithologies are mainly gray gneisses that are strongly
87   foliated and locally migmatized with quartzofeldspathic bands and thin biotite-rich layers. The
88   biotite–tremolite schist sample comes from an inclusion in the TTG gneiss (Figure 2a,d), and
89   the granitic gneisses at this location form sheet-like intrusions that cut across the other TTG
90   gneisses (Figure 2e,f). The data for other samples such as PM51-6-1, PM51-6-2, PM51-6-3, D050-
91   1, and D050-2, included on some of the later figures, are from the unpublished data of Yunxu
92   Wei.

93
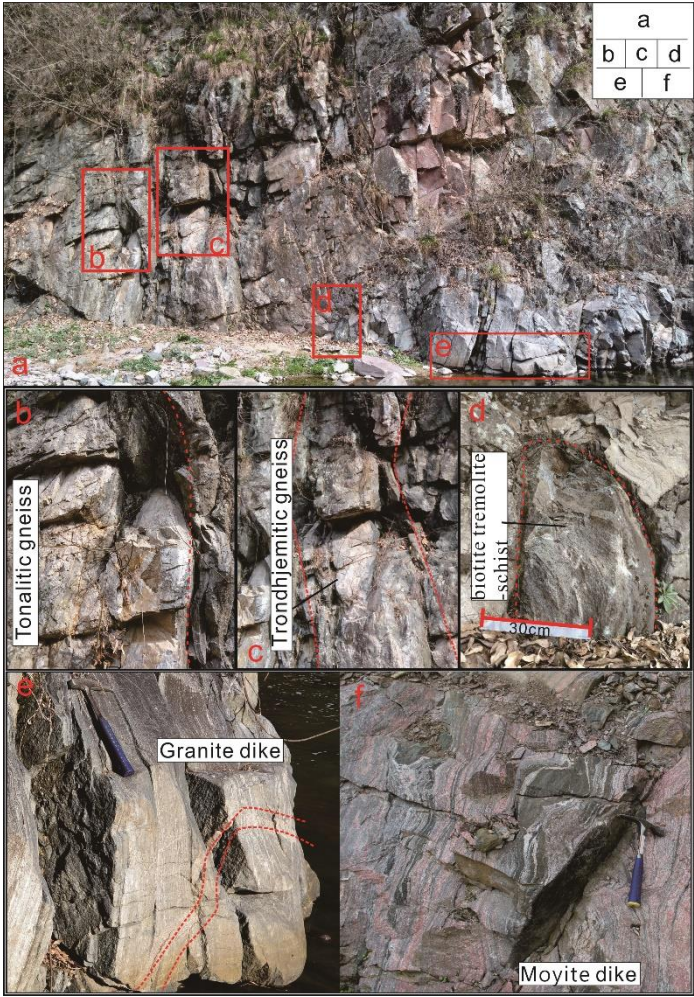
94   **Figure 2.** Field photographs of the Shuiyuesi granite–greenstone terrane showing outcrops of
95   (a) the Taoyuan trondhjemite gneiss, (b) the tonalitic gneiss, (c) the trondhjemitic gneiss, (d)
96   the biotite–tremolite schist, (e) a granite dike, and (f) the moyite dike.

97   2.2.1. TTG

98   The TTG samples are medium- to fine-grained, gneissose, and composed mainly of
99   plagioclase, quartz, K-feldspar, and biotite. The plagioclase content is 60%–70%, polysynthetic
100   twinning is visible, and the crystals show obvious K-metasomatism with visible reaction rims
101   of K-feldspar. Most surfaces of the plagioclase are pitted with sericite and biotite alteration.
102   Anhedral quartz makes up 10%–15% of TTG rocks, and it forms irregular aggregates of
103   granular grains in the size range of 0.2–0.8 mm. The platy biotite that makes up 5%–10% of the
104   rock occurs as dispersed grains that have been altered to muscovite and sericite. Less abundant
105   K-feldspar and other minerals, such as epidote, are also present (Figure 3a,b).

106   2.2.2. granite dikes

107   The granite dikes are made up of plagioclase, quartz, K-feldspar, and lesser amounts of
108   biotite. The K-feldspar is anhedral and granular, and shows cross-hatched twinning. Sample
109   D0002-5 underwent K-feldspathization and has a high K-feldspar content of 70%. Small
110   amounts of epidote are also present (Figure3c).

111
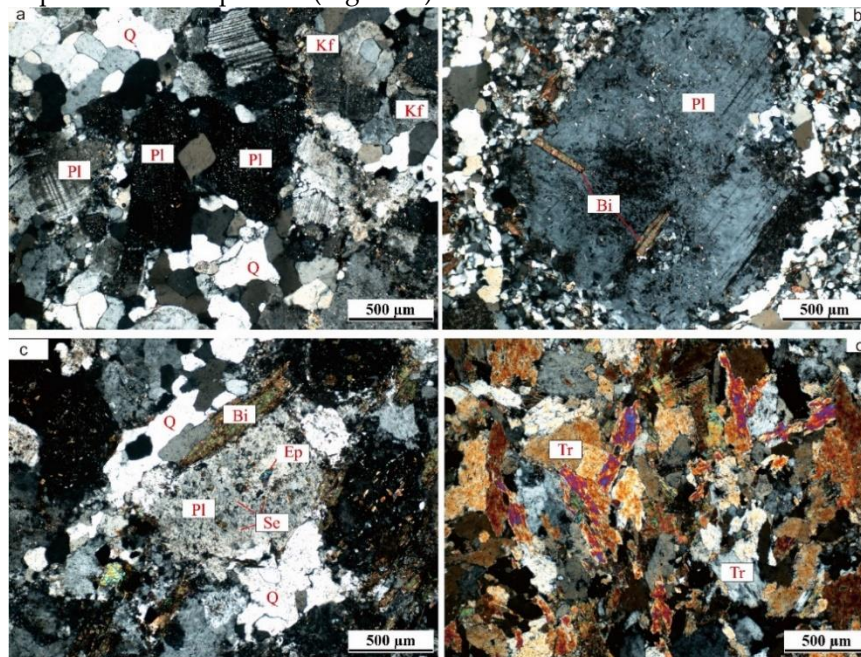
112   **Figure 3.** Photomicrographs of the TTG gneiss and biotite–tremolite schist in the Northern
113   Kongling Terrane. (a): Sample D0002-2; (b): Sample SMK-1; (c): Sample D0002-4; (d): Sample
114   D0002-1.

115   2.2.3. biotite–tremolite schist

116   The biotite–tremolite schist has a crystalloblastic texture and schistose structure, with
117   biotite (Bi) and tremolite (Tr) as the main minerals, along with some dolomite and magnetite.
118   The tremolite is euhedral, columnar, and colorless, and the long axes of the crystals show a
119   preferred orientation (Figure 3d). The tremolite grains are 0.2–2.0 mm in size and make up
120   60%–65% of the rock. The 0.2–2.0 mm grains of biotite are euhedral, platy, and yellowish green,
121   and they display a preferred orientation (Figure 3d). The biotite makes up about 30%–35% of
122   the rock. The 0.1–0.2 mm grains of granular dolomite fill the spaces between the tremolite and
123   biotite. They make up 3%–4% of the rock.

3. Analytical Methods

3.1. Zircon Morphology

Sample processing for zircon separation involved crushing, initial heavy liquid separation and subsequent magnetic separation. Representative zircons were hand-picked and mounted on adhesive tape, embedded in epoxy resin, polished to about half their size and photographed in reflected and transmitted light (Song et al., 2002). CL images were used to reveal the internal structures of zircons and to help select optimum spot locations for later in situ analysis. The imaging was done at the State Key Laboratory of Continental Dynamics, Xi'an and the State Key Laboratory of Geological Processes. The laboratory in Xi'an uses a FEI Quanta 400 FEG high resolution emission field environmental scanning electron microscope connected to an Oxford INCA350 energy dispersive system (EDS) and a Gatan Mono CL3+ system. The working distance for the CL system was 8.4 mm, while the EDS used a spot size of 6.7 nm with a voltage of 10 kV.

3.2. Zircon U–Pb Dating

Laser ablation ICP-MS zircon U–Pb analyses were conducted on an Agilent 7500a ICP-MS equipped with a 193 nm laser, which is housed at the Department of Geology, Northwest University in Xi'an, China. During analysis, the spot diameter was 30 μm. Raw count rates for ^{29}Si, ^{204}Pb, ^{206}Pb, ^{207}Pb, ^{208}Pb, ^{232}Th and ^{238}U were collected for age determination. U, Th and Pb concentrations were calibrated by using ^{29}Si as the internal calibrant and NIST 610 as the reference material. The $^{207}Pb/^{206}Pb$ and $^{206}Pb/^{238}U$ ratios were calculated using the GLITTER program, which were then corrected using the Harvard zircon 91500 as external calibrant. According to the method of Ballard, Palin [24], measured $^{207}Pb/^{206}Pb$, $^{206}Pb/^{238}U$ and $^{208}Pb/^{232}Th$ ratios in zircon 91500 were averaged over the course of the analytical session and used to calculate correction factors. These correction factors were then applied to each sample to correct for both instrumental mass bias and depth-dependent elemental and isotopic fractionation. The detailed analytical technique is described in Yuan, Gao [25]. The ^{204}Pb isotope cannot be precisely measured with this technique, due to a combination of low signal and interference from small amounts of ^{204}Hg in the Ar gas supply. Common Pb contents were therefore evaluated using the method described by Andersen [26]. The age calculations and plotting of concordia diagrams were made using ISOPLOT (ver 3.15)[27]. The errors quoted in tables and figures are at the 2σ levels.

3.3. Major and Trace Element Analyses

Whole-rock samples were crushed in a corundum jaw crusher (to a size of 60 mesh). About 60 g was powdered in an agate ring mill to a size of less than 200 mesh. Major element contents of the samples were determined by X-ray fluorescence analysis of fused glass beads using a spectrometer (3080E1; Rigaku, Tokyo, Japan) and trace elements were determined on the ICP MS (X.series, Thermo Fisher Scientific, Germany) at the Wuhan Rock and Mineral Analysis Center, Ministry of Land and Resources Research, China. Analytical precision and accuracy with these methods are better than 5% for most elements. The ferric–ferrous iron proportions were determined by wet chemistry.

3.4. Zircon Lu–Hf Isotope Analysis

Experiments were conducted using a Neptune Plus MC-ICP MS (Thermo Fisher Scientific, Germany) in combination with a Geolas 2005 ArF-excimer laser ablation system (Lambda Physik, Göttingen, Germany) that was hosted at the state Key Laboratory of Geological Processes and Mineral Resources, China University of Geosciences in Wuhan. The energy density of laser ablation used in this study was 5.3 J/cm². A 'wire' signal smoothing device is

170 included in this laser ablation system, ensuring the production of smooth signals at even very
171 low laser repetition rates down to 1Hz [28, 29]. Detailed operating conditions for the laser
172 ablation system and the MC-ICP MS instrument, along with the analytical methods, are
173 described in Hu, Liu [28].

174 **4. Results**

175 *4.1. Zircon U–Pb ages*

176 4.1.1. Biotite tremolite schist

177 The zircon grains from the biotite–tremolite schist (D0002-1) are subhedral to anhedral
178 and can be classified into two types based on their CL images. Most grains show oscillatory
179 zoning typical of magmatic zircons. The other zircon grains (red circles) display obvious
180 metamorphic core structures (Figure 4).

181
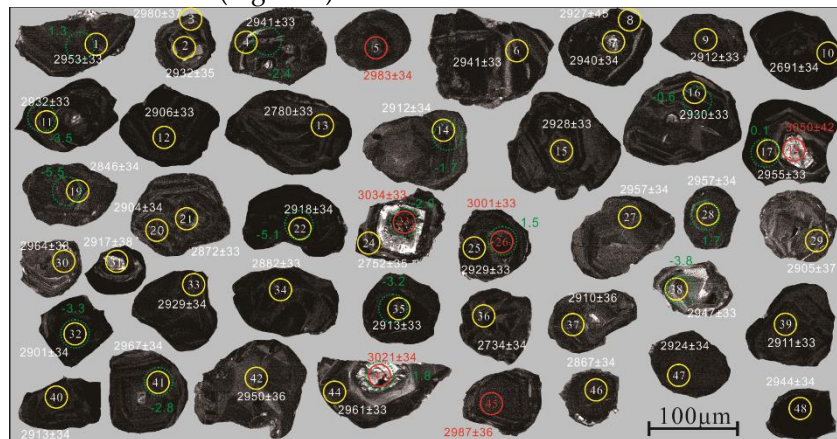
182 **Figure 4.** Representative cathodoluminescence images of zircons from the biotite–tremolite
183 schist (D0002-1). The yellow circles show the locations of the LA–ICP–MS U–Pb analyses. The
184 white number in each circle is the number of the analysis. The white number outside each circle
185 is the age (Ma) for each site. The red circles and numbers give the analysis numbers and ages
186 (Ma) for the smaller relict cores in those complex zircons.

187 Forty-eight spots on 41 grains were analyzed (Figure 4), and 13 of the U–Pb isotopic data
188 are discordant (Figure 5a), suggesting Pb loss caused by a later metamorphic event. These
189 analyses, combined with six concordant spots, form a discordia line that yields an upper
190 intercept $^{207}Pb/^{206}Pb$ age of 2994 ± 26 Ma (2σ, MSWD = 6.1, n = 19). The six concordant spots
191 yield a weighted mean $^{207}Pb/^{206}Pb$ age of 3011 ± 27 Ma (2σ, MSWD = 2.1, n = 6). The remaining
192 29 spots with ages of 2967–2901 Ma fall close to the upper intercept, are nearly concordant
193 (concordance >98%), and give a weighted mean $^{207}Pb/^{206}Pb$ age of 2933 ± 13 Ma (2σ, MSWD =
194 0.34, n = 29).
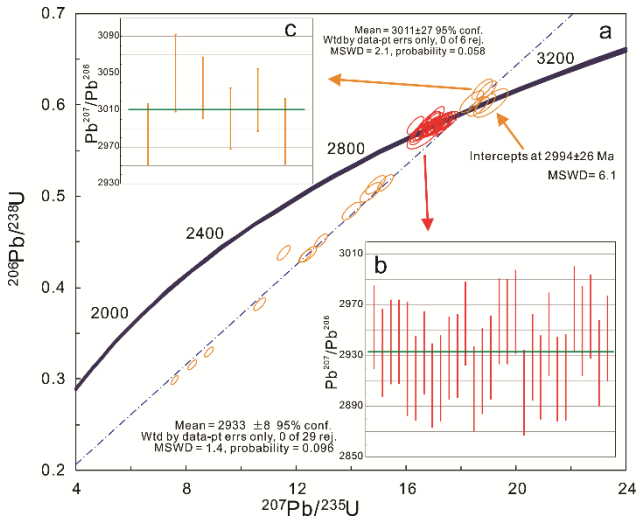
Figure 5. Zircon U–Pb age diagrams for the biotite–tremolite schist (D0002-1). (a) Orange circles for all analyzed spots (n = 19) with a discordia curve that shows an upper intercept age of 2994 ± 26 Ma (MSWD = 6.1). Red circles for a concordia curve (n = 29) yield an age of 2940 ± 19 Ma (MSWD = 0.42). (b) Weighted mean values for all spots with concordant ages (n = 29). The mean age is 2933 ± 8 Ma (MSWD = 1.4). (c) Weighted mean values for six spots that yield a concordant age of 3011 ± 27 Ma (MSWD = 2.1)

Table 1 Representative major (wt. %) and trace element (ppm) concentrations of the Biotite tremolite-schist, Archean TTG and dikes in Northern Kongling terrain.

Sample	D0002-1 Bi-Ttremolite-schist	D0002-2	SMK-4	D0002-3	SMK-1	D0002-4	D0002-5
		Tonalitic gneiss		Trondhjemite gneiss		Granite dike	
SiO_2	54.71	76.80	70.86	76.08	69.79	73.92	78.74
TiO_2	0.24	0.09	0.29	0.16	0.43	0.18	0.03
Al_2O_3	2.78	13.77	15.82	14.08	15.49	13.11	12.85
FeO_{total}	6.65	0.55	2.05	0.57	2.19	1.12	0.24
MnO	0.24	0.01	0.03	0.01	0.03	0.02	0.01
MgO	20.81	0.29	0.81	0.30	1.02	0.28	0.16
CaO	10.28	0.91	2.82	0.75	2.48	1.21	0.85
Na_2O	0.11	5.98	4.98	6.67	4.55	4.41	5.98
K_2O	1.46	0.88	1.53	0.70	2.62	4.28	0.52
P_2O_5	0.01	0.02	0.06	0.05	0.12	0.08	0.02
LOI	1.53	0.49	0.37	0.47	0.71	0.98	0.47
Total	98.82	99.78	99.62	99.84	99.43	99.59	99.87
Mg#	85.00	47.00	41.00	47.00	45.00	30.00	55.00
K_2O+Na_2O	1.57	6.86	6.51	7.37	7.17	8.69	6.50
K_2O/Na_2O	12.80	0.15	0.31	0.11	0.58	0.97	0.09
A/CNK	0.14	1.11	1.06	1.07	1.05	0.93	1.08
V	56.4	7.68	19.66	8.38	43.64	18.4	4.1
Cr	1800	3.39	9.48	1.7	12.32	6.66	1.52
Co	106	1.52	55.49	1.33	61.78	2.13	<1
Ni	1630	2.87	7.17	3.14	8.41	4.88	3.29
Ga	7.5	33.6	15.24	20.8	53.29	63.6	24.5
Rb	94.7	23.4	75.44	26.3	56.78	76.5	16.5
Sr	20.5	311	370.39	196	437.36	243	342
Y	5.9	7.89	6.27	4.82	9.28	10.6	12.2
Zr	29.8	66.1	102.94	91.6	248.84	215	61.7
Nb	1.26	3.1	6.66	3.01	6.1	2.8	2.74
Ba	121	947	186.83	312	159.08	2540	306
La	1.19	28.6	18.5	14.8	24.32	148	15.8
Ce	3.05	39.7	29.38	19.6	39.93	195	20.4
Pr	0.62	5.53	3.33	2.76	5.05	18.1	2.98
Nd	3.07	20	11.18	10	18.31	60.4	11.6
Sm	0.88	3.47	1.65	1.76	3.12	8.37	2.55
Eu	0.24	1.05	0.74	0.8	1.49	1.69	0.7
Gd	0.86	2.79	1.42	1.55	2.74	6.67	2.29
Tb	0.16	0.34	0.2	0.22	0.35	0.66	0.38
Dy	1.1	1.6	1.13	1.08	1.81	2.46	2.28
Ho	0.24	0.29	0.23	0.19	0.34	0.41	0.46
Er	0.64	0.76	0.73	0.46	0.97	1.04	1.24
Tm	0.1	0.11	0.12	0.062	0.14	0.11	0.2
Yb	0.71	0.74	0.87	0.36	0.92	0.68	1.29
Lu	0.1	0.1	0.14	0.044	0.14	0.086	0.18
Hf	0.98	2.99	3.21	2.88	6.29	5.29	4.45
Ta	0.099	0.41	0.56	0.088	0.54	0.097	0.43
Pb	3.38	8.71	19.4	5.88	19.27	12.4	10.8
Th	0.19	12.5	4.95	1.63	7.26	11.5	13.6
U	0.42	1.6	0.41	0.36	1	0.49	5.49
La_N/Yb_N	1.2	27.72	15.3	29.49	18.88	156.12	8.79
Eu/Eu*	0.83	1	1.42	1.45	1.52	0.67	0.87
1000 Ga/Al	5.4	4.88	0.36	2.95	0.32	9.7	3.81
Total REE	12.96	105.08	69.62	53.69	99.65	443.68	62.35

205 **Table 2 Lu-Hf isotope data for zircons from the Biotite tremolite-schist, Archean TTG and dikes in Nor**thern Kongling terrain.

Sample	$^{176}Hf/^{177}Hf$	1σ	$^{176}Lu/^{177}Hf$	1σ	$^{176}Yb/^{177}Hf$	1σ	Age (Ma)	$^{176}Hf/^{177}Hf$ (t)	$\varepsilon_{Hf}(t)$	1σ	T_{DM1}	T_{DM2}	$f_{Lu/Hf}$
D0002-1-01	0.280951	0.000022	0.000407	0.000002	0.008177	0.000031	2953	0.280927	1.3	1.1	3.15	3.23	-0.99
D0002-1-02	0.280855	0.000014	0.000404	0.000003	0.008611	0.000039	2941	0.280833	-2.4	0.9	3.27	3.41	-0.99
D0002-1-03	0.280835	0.000012	0.000486	0.000004	0.010876	0.000113	2932	0.280808	-3.5	0.8	3.31	3.46	-0.99
D0002-1-04	0.280890	0.000018	0.000327	0.000002	0.006678	0.000024	2912	0.280872	-1.7	1.0	3.22	3.35	-0.99
D0002-1-05	0.280916	0.000024	0.000474	0.000003	0.010331	0.000080	2930	0.280890	-0.6	1.1	3.20	3.31	-0.99
D0002-1-06	0.280917	0.000018	0.000384	0.000005	0.008261	0.000050	2955	0.280895	0.1	1.0	3.19	3.29	-0.99
D0002-1-07	0.280838	0.000010	0.000536	0.000003	0.012015	0.000112	2846	0.280809	-5.5	0.8	3.31	3.50	-0.98
D0002-1-08	0.280786	0.000012	0.000260	0.000004	0.005863	0.000093	2918	0.280771	-5.1	0.8	3.35	3.54	-0.99
D0002-1-09	0.280869	0.000011	0.001473	0.000064	0.048796	0.002518	3034	0.280784	-2.0	0.9	3.35	3.46	-0.96
D0002-1-10	0.280926	0.000018	0.000423	0.000006	0.010519	0.000087	3001	0.280902	1.5	1.0	3.18	3.26	-0.99
D0002-1-11	0.280961	0.000015	0.000399	0.000004	0.009691	0.000113	2957	0.280939	1.7	0.9	3.13	3.21	-0.99
D0002-1-12	0.280875	0.000012	0.000721	0.000002	0.017945	0.000048	2901	0.280834	-3.3	0.8	3.27	3.43	-0.98
D0002-1-13	0.280877	0.000012	0.000847	0.000006	0.020028	0.000231	2913	0.280830	-3.2	0.8	3.28	3.43	-0.97
D0002-1-14	0.280822	0.000016	0.000556	0.000003	0.013783	0.000090	2947	0.280790	-3.8	0.9	3.33	3.49	-0.98
D0002-1-15	0.280831	0.000012	0.000460	0.000003	0.010361	0.000129	2967	0.280804	-2.8	0.8	3.31	3.45	-0.99
D0002-1-16	0.280883	0.000013	0.001490	0.000040	0.052002	0.001677	3021	0.280797	-1.8	0.9	3.33	3.44	-0.96
D0002-2-01	0.280847	0.000010	0.000733	0.000002	0.022362	0.000070	2934	0.280806	-3.5	0.8	3.31	3.47	-0.98
D0002-2-02	0.280872	0.000013	0.001010	0.000010	0.029241	0.000148	2945	0.280815	-3.0	0.9	3.30	3.44	-0.97
D0002-2-03	0.280859	0.000015	0.001520	0.000031	0.045511	0.000942	2956	0.280772	-4.2	0.9	3.36	3.52	-0.95
D0002-2-04	0.280853	0.000012	0.001015	0.000017	0.030518	0.000620	2958	0.280796	-3.3	0.9	3.33	3.47	-0.97
D0002-2-05	0.280844	0.000011	0.000784	0.000036	0.022883	0.001178	2951	0.280800	-3.3	0.9	3.32	3.47	-0.98
D0002-2-06	0.280870	0.000014	0.001882	0.000044	0.057025	0.001497	2948	0.280763	-4.7	0.9	3.38	3.54	-0.94
D0002-2-07	0.280841	0.000015	0.001046	0.000017	0.030454	0.000321	2952	0.280782	-4.0	0.9	3.35	3.50	-0.97
D0002-2-08	0.280868	0.000012	0.001518	0.000031	0.046408	0.001013	2941	0.280783	-4.2	0.9	3.35	3.51	-0.95
D0002-3-01	0.280909	0.000015	0.001418	0.000024	0.043538	0.000698	2992	0.280828	-1.4	0.9	3.29	3.40	-0.96
D0002-3-02	0.280843	0.000013	0.001184	0.000014	0.034520	0.000424	2925	0.280776	-4.8	0.9	3.36	3.52	-0.96
D0002-3-05	0.280889	0.000015	0.001882	0.000014	0.058348	0.000387	2988	0.280781	-3.2	0.9	3.36	3.49	-0.94

D0002-3-06	0.280793	0.000009	0.000684	0.000016	0.020283	0.000417	3009	0.280754	-3.6	0.8	3.38	3.53	-0.98
D0002-3-07	0.280870	0.000013	0.001423	0.000015	0.042550	0.000518	2945	0.280790	-3.8	0.9	3.34	3.49	-0.96
D0002-3-08	0.280844	0.000013	0.000642	0.000012	0.019083	0.000451	2984	0.280807	-2.3	0.9	3.31	3.44	-0.98
D0002-3-09	0.280867	0.000015	0.001473	0.000006	0.043742	0.000368	2939	0.280784	-4.2	0.9	3.35	3.50	-0.96
D0002-4-01	0.280900	0.000013	0.001646	0.000045	0.050871	0.001707	2964	0.280807	-2.8	0.9	3.32	3.45	-0.95
D0002-4-02	0.280856	0.000011	0.000579	0.000006	0.017595	0.000264	2872	0.280824	-4.3	0.8	3.29	3.46	-0.98
D0002-4-03	0.280913	0.000016	0.001225	0.000019	0.040155	0.000434	2933	0.280844	-2.2	0.9	3.27	3.39	-0.96
D0002-4-04	0.280813	0.000012	0.001099	0.000020	0.029884	0.000733	2952	0.280751	-5.1	0.9	3.39	3.56	-0.97
D0002-4-05	0.280910	0.000011	0.001667	0.000033	0.049941	0.001195	2880	0.280818	-4.3	0.8	3.31	3.47	-0.95
D0002-4-06	0.280897	0.000012	0.001006	0.000013	0.031209	0.000358	2942	0.280840	-2.1	0.9	3.27	3.40	-0.97
D0002-4-07	0.280880	0.000011	0.000942	0.000004	0.028800	0.000249	2934	0.280827	-2.8	0.8	3.29	3.43	-0.97
D0002-4-08	0.280874	0.000012	0.001062	0.000011	0.032768	0.000244	2936	0.280814	-3.2	0.8	3.30	3.45	-0.97
D0002-4-09	0.280830	0.000015	0.001237	0.000021	0.037397	0.000921	2956	0.280760	-4.6	0.9	3.38	3.54	-0.96
D0002-4-10	0.280907	0.000011	0.001973	0.000013	0.065697	0.000407	2884	0.280798	-4.9	0.8	3.34	3.50	-0.94
D0002-4-11	0.280879	0.000012	0.001324	0.000009	0.041879	0.000096	2953	0.280804	-3.1	0.9	3.32	3.46	-0.96
D0002-4-12	0.280941	0.000012	0.002114	0.000107	0.070993	0.004036	2935	0.280822	-2.9	1.0	3.30	3.43	-0.94
D0002-4-13	0.280908	0.000012	0.001696	0.000029	0.051172	0.001052	2887	0.280814	-4.3	0.9	3.31	3.47	-0.95
D0002-4-14	0.280879	0.000009	0.001193	0.000021	0.034871	0.000890	2887	0.280813	-4.4	0.8	3.31	3.47	-0.96
D0002-5-01	0.280920	0.000020	0.001397	0.000015	0.038193	0.000434	2909	0.280842	-2.8	1.0	3.27	3.41	-0.96
D0002-5-02	0.280888	0.000010	0.001054	0.000016	0.030283	0.000378	2877	0.280830	-4.0	0.8	3.28	3.44	-0.97
D0002-5-03	0.280845	0.000013	0.000937	0.000020	0.028552	0.000584	2859	0.280793	-5.7	0.9	3.33	3.52	-0.97
D0002-5-04	0.280900	0.000024	0.001250	0.000008	0.034076	0.000142	2887	0.280830	-3.7	1.1	3.29	3.44	-0.96
D0002-5-05	0.280909	0.000018	0.001086	0.000031	0.030378	0.000766	2920	0.280848	-2.3	1.0	3.26	3.39	-0.97
D0002-5-06	0.280859	0.000009	0.001239	0.000027	0.039478	0.000984	2879	0.280790	-5.4	0.8	3.34	3.52	-0.96
D0002-5-07	0.280880	0.000012	0.001151	0.000012	0.032658	0.000295	2906	0.280816	-3.8	0.8	3.30	3.46	-0.97
D0002-5-08	0.280869	0.000017	0.000540	0.000007	0.015970	0.000183	2868	0.280839	-3.9	0.9	3.27	3.43	-0.98

206 Note: a, Initial Hf isotope ratios are calculated nearly by their Age of single grain zircon; b, T_{DM2} are calculated by assuming a mean $^{176}Lu/^{177}Hf$ value of 0.015 for the average continental crust[30].

207

4.1.2. TTG Gneiss

The zircon grains from the tonalitic gneiss (D0002-2) have different features from the zircons of the biotite–tremolite schist sample D0002-1, described above. Thirty spots on 25 grains were analyzed (Table S2), and most of the U–Pb isotopic data are discordant (Figure 7). All analyzed spots gave an upper intercept age of 2943 ± 15 Ma (MSWD = 8.4, n = 25), and eight of the grains form a tight population with a weighted mean ^{207}Pb/^{206}Pb age of 2948 ± 26 Ma (MSWD = 0.053, n = 8) and a concordant age of 2947 ± 5.6 Ma (MSWD = 0.006), which is within error of the U–Pb age of 2944 ± 22 Ma for zircons from the biotite–tremolite schist (sample D0002-1).

Figure 6. Representative cathodoluminescence images of zircons from the tonalitic gneiss (D0002-2). Symbols are as in Figure 4.
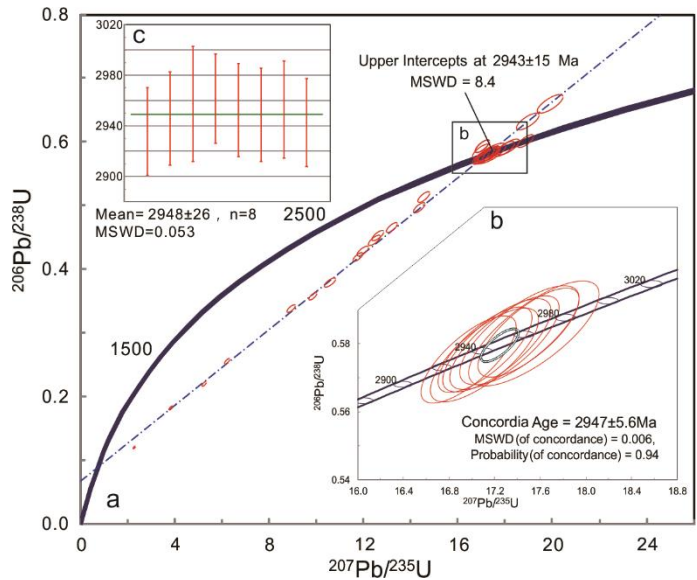
Figure 7. Zircon U–Pb concordia age diagram for the tonalitic gneiss (D0002-2). (a) Diagram for all analytical spots that gave a discordia line with an upper intercept ^{207}Pb/^{206}Pb age of 2943 ± 15 Ma. (b) and (c) Diagrams for eight analytical spots that gave a concordant ^{207}Pb/^{206}Pb age of 2947 ± 5.6 Ma and a weighted mean ^{207}Pb/^{206}Pb age of 2948 ± 26 Ma.

225   Zircon grains from the trondhjemitic gneiss (D0002-3) are euhedral to subhedral, slightly
226   rounded in form, and display oscillatory zoning in CL images, typical of magmatic zircons
227   (Figure 8). Most of the zircon grains display core–rim structures. The rims are usually very
228   narrow, dark, and structureless, suggesting recrystallization during a later hydrothermal
229   alteration. These rims were too narrow to be analyzed. Thirty spots on 22 grains were analyzed
230   (Table S3), and most of the U–Pb isotopic data are discordant (Figure 9a), suggesting Pb loss
231   caused by a later hydrothermal event. A discordia line of 14 discordant analyses yielded an
232   upper intercept $^{207}Pb/^{206}Pb$ age of 3007 ± 18 Ma (2σ, MSWD = 3, n = 14). The remaining 16 spots
233   with ages of 2955–2899 Ma are nearly concordant (concordance >98%), and they gave a
234   concordant age of $^{207}Pb/^{206}Pb$ age of 2939 ± 4 Ma (2σ, MSWD = 0.18, n = 16; Figure 9b) and a
235   weighted mean $^{207}Pb/^{206}Pb$ age of 2935 ± 9 Ma (2σ, MSWD = 0.6, n = 16; Figure 9c).

236

237   **Figure 8.** Representative cathodoluminescence images of zircons from the trondhjemitic gneiss
238   (D0002-3). Symbols are as in Figure 4.

239
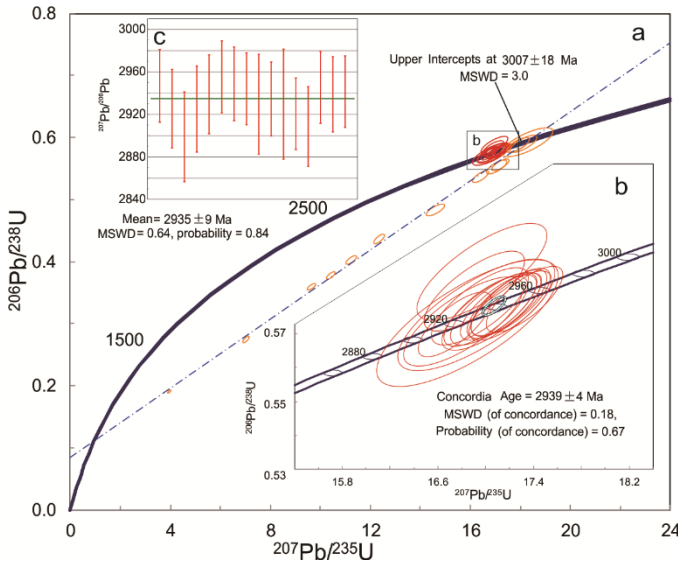
240   **Figure 9.** Zircon U–Pb concordia age diagrams for the trondhjemitic gneiss (D0002-3). (a)
241   Diagram for 14 analytical spots that gave a discordia line with an upper intercept $^{207}Pb/^{206}Pb$
242   age of 3007 ± 18 Ma. (b) and (c) Diagrams for 16 analytical spots that gave a concordant
243    $^{207}Pb/^{206}Pb$ age of 2939 ± 4 Ma and a weighted mean $^{207}Pb/^{206}Pb$ age of 2935 ± 9 Ma.

244

245   4.1.3. Granite Dikes

246   The zircon grains from the dikes of gneissic granite (D0002-4) are subhedral to anhedral
247   (Figure 10). Most of the zircons display core–rim structures, and they can be divided into two
248   groups by the internal textures of the cores. In group a, the cores have a complicated internal
249   texture with sector zoning but no oscillatory zoning, suggesting a metamorphic origin. In
250   contrast, the zircons of group b display weak sector zoning and obvious oscillatory zoning that
251   is typical of magmatic zircons.

252   Thirty-six spots were analyzed (Table S4), and two discordia lines are present in the zircon
253   U–Pb concordia age diagrams for sample D00002-4. The one discordia line with 18 discordant
254   analyses yielded an upper intercept $^{207}Pb/^{206}Pb$ age of 2881 ± 15 Ma (2σ, MSWD = 0.50, n = 16;
255   Figure 11a), and five analyses gave a concordant age of $^{207}Pb/^{206}Pb$ age of 2882 ± 15 Ma (2σ,
256   MSWD = 0.13, n = 5; Figure 11b). The other discordia line with 18 analyses defined an older
257   upper intercept $^{207}Pb/^{206}Pb$ age of 2944 ± 9 Ma (2σ, MSWD = 0.5, n = 18) and a weighted mean
258   $^{207}Pb/^{206}Pb$ age of 2943 ± 10 Ma (2σ, MSWD = 0.39, n = 10; Figure 11c).

259

260   **Figure 10.** Representative cathodoluminescence images of zircons from the granite dike
261   (D0002-4). Symbols are as in Figure 4.

262
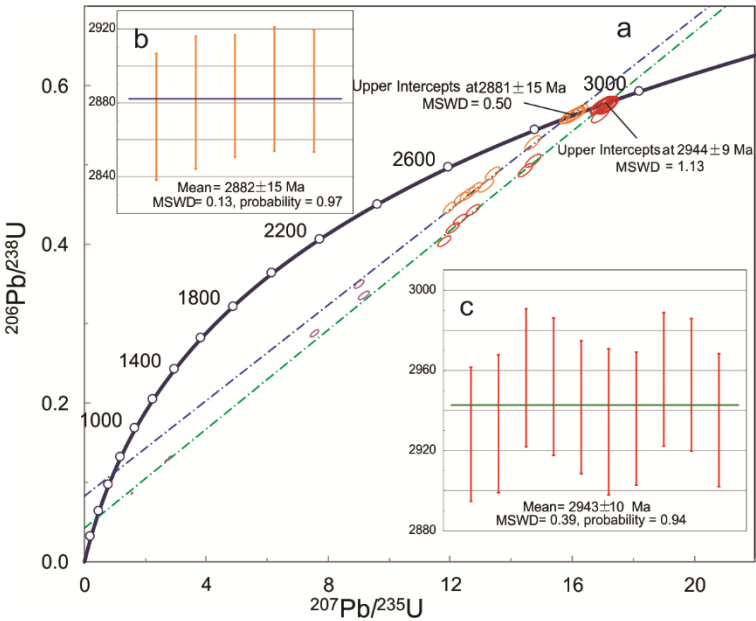
263   **Figure 11.** Zircon U–Pb concordia age diagrams for the granite dike (D0002-4). (a) Diagram for
264   all analyzed spots that gave two discordia lines with upper intercept ^{207}Pb/^{206}Pb ages of 2994 ±
265   9 Ma and 2881 ± 15 Ma. (b) Diagram for five concordant analyses that gave a weighted mean
266   ^{207}Pb/^{206}Pb age of 2882 ± 15 Ma. (c) Diagram for 10 concordant analyses that gave a weighted
267   mean ^{207}Pb/^{206}Pb age of 2943 ± 10 Ma.

268   The zircon grains from the moyite dike (D0002-5) (Figure 12) are smaller but otherwise
269   similar to those from granite dike D0002-4. Twenty-four spots on 22 grains were analyzed
270   (Table S5), and most of the U–Pb isotopic data were discordant (Figure 13a), suggesting Pb loss
271   caused by a later hydrothermal event. A discordia line with 16 discordant analyses yielded an
272   upper intercept ^{207}Pb/^{206}Pb age of 2874 ± 11 Ma (2σ, MSWD = 0.43, n = 16), and another 5 analyses
273   gave a concordant ^{207}Pb/^{206}Pb age of 2874 ± 15 Ma (2σ, MSWD = 0.42, n = 3; Figure 13b). The
274   remaining eight spots defined an older upper intercept ^{207}Pb/^{206}Pb age of 2910 ± 11 Ma (2σ,
275   MSWD = 0.49, n = 8) and a weighted mean ^{207}Pb/^{206}Pb age of 2911 ± 19 Ma (2σ, MSWD = 0.20, n
276   = 3; Figure 13c).

277

278   **Figure 12.** Representative cathodoluminescence images of zircons from the moyite dike
279   (D0002-5). Symbols are as in Figure 4.

280
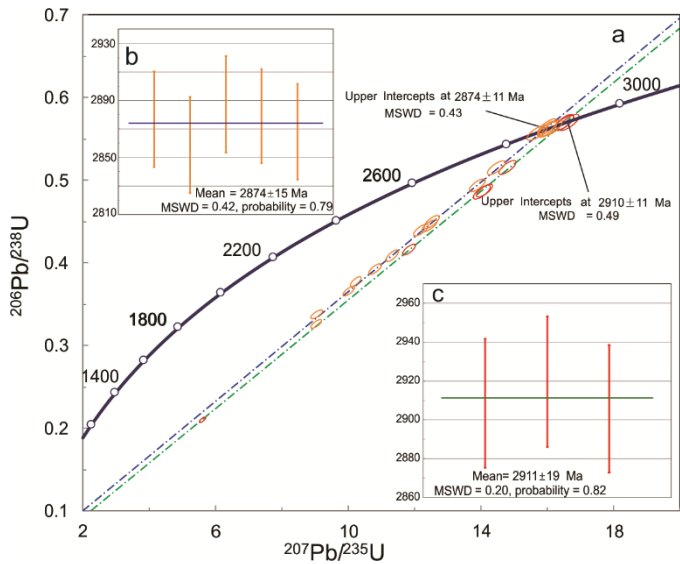
281   **Figure 13.** Zircon U–Pb concordia age diagrams for the moyite dike (D0002-5). (a) Diagram for
282   all analyzed spots that gave two discordia lines with two upper intercept ^{207}Pb/^{206}Pb ages of
283   2910 ± 11 Ma and 2874 ± 11 Ma. (b) Diagram for five concordant analyses that gave a weighted
284   mean ^{207}Pb/^{206}Pb age of 2874 ± 15 Ma. (c) Diagram for three concordant analyses that gave a
285   weighted mean ^{207}Pb/^{206}Pb age of 2911 ± 19 Ma.

286   *4.2. Whole-rock major and trace element compositions*

287   4.2.1. Biotite Tremolite-schist

288   The results of the major and trace element analyses of the five samples are presented in
289   Table 6. The samples from the Yemadong Group display relatively low contents of SiO_2 (30.24–
290   54.71 wt%, average 46.23 wt%) and Al_2O_3 (2.78–6.36 wt%, average 5.01 wt%), but relatively high
291   contents of MgO (19.27–27.01 wt%, average 22.88 wt%). The samples can be divided into two
292   series by their total alkali contents ($Na_2O + K_2O$). The three samples of the first series (D050-1,
293   D050-2, and D0002-1) have relatively high total alkali contents (1.57–3.69 wt%, average 2.86
294   wt%), and the other two samples display lower contents (0.29 wt% and 0.41 wt%).

295
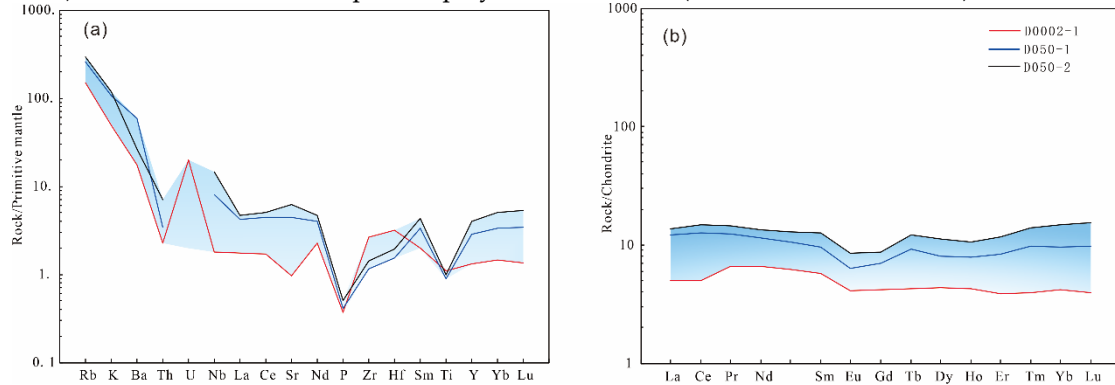
296   **Figure 14.** (a) Primitive-mantle-normalized trace element distributions and (b) chondrite-
297   normalized rare earth element patterns for the biotite–tremolite schist enclaves from the
298   Kongling Terrane. Normalizing values are from McDonough and Sun (1989).

299   The trace element compositions of the first series of samples (D050-1, D050-2, and D0002-
300   1) show strong enrichments in large ion lithophile elements (LILEs; e.g., K, Rb, Ba, and Th) and
301   depletions in high field strength elements (HFSEs; e.g., Nb, Ta, P, and Ti; Figure 14a). The other
302   two samples show depletions in LILEs and enrichments in HFSEs. All five samples have very
303   high Cr (>1300 ppm) and Ni (>800 ppm) contents.

304   In summary, the biotite–tremolite schists possess lower total REE values (9.46–33.12 ppm),
305   relatively flat REE patterns (average $(La/Yb)_N$ ratio of 0.99; Figure 14b), and both positive and
306   negative Eu anomalies (δEu = 0.73–1.40). The protoliths of the biotite–tremolite schists were
307   basic–intermediate magmatic rocks of the calc-alkaline series, including subAlkaline basalt,
308   basalt, or basaltic andesite (Figure 15a). On a TFeO.MgO vs SiO_2 volcanic rock classification
309   diagram, all the Archean metabasite samples fall into calc-alkaline series fields.

310
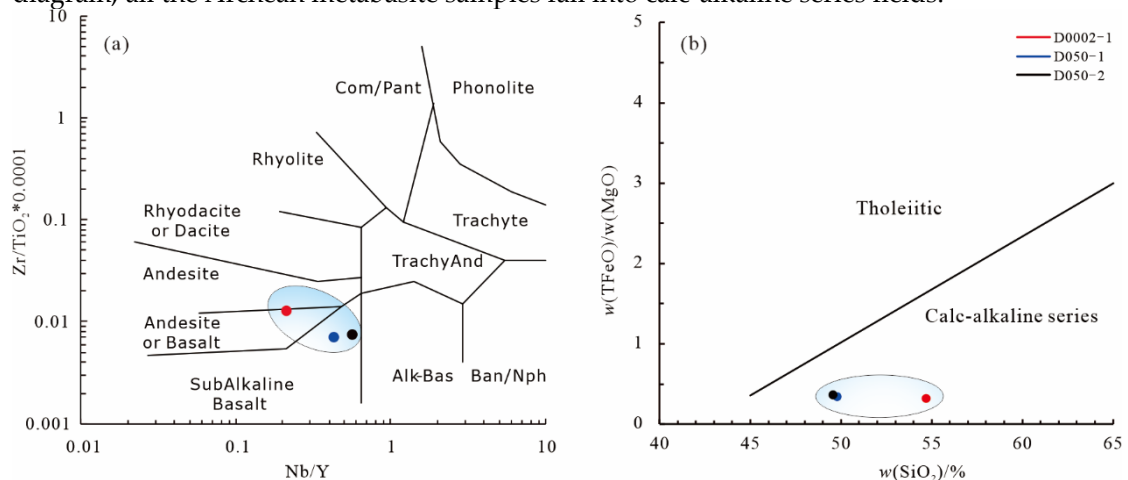
311   **Figure 15. a,**Classification of the biotite–tremolite schist enclaves from the Kongling Terrane
312   using the Nb/Y vs Zr/Ti diagram after [31] and modified by[32]; b, TFeO.MgO vs SiO₂ diagram
313   after [33]

4.2.2. TTG Gneiss and dikes

315   The major and trace element compositions of the TGG gneissic rocks are listed in Table 6.
316   According to their normative feldspar compositions, two samples are recognized as
317   trondhjemites, sample SMK-1 falls near the granodiorite field, and sample SMK-4 falls close to
318   the tonalite field (Figure 16a). All the samples display relatively high contents of SiO_2 (69.79–
319   76.80 wt%, Figure 16b), Al_2O_3 (13.77–15.82 wt%, Figure 17), and total alkalis ($Na_2O + K_2O$; 6.51–
320   7.37 wt%), high values of $Mg^\#$ (41–47), and comparatively low contents of K_2O (0.70–2.62 wt%,
321   Figure 17), TiO_2 (0.09–0.43 wt%, Figure 17), FeO^T (0.55–2.19 wt%, Figure17), and MgO (0.29–
322   1.02 wt%) (Figure 17c). They are magnesian and weakly peraluminous (A/CNK 1.05–1.11)
323   (Figure 16b). In the $FeOt/(FeOt+MgO)$-SiO_2 classification diagram, and granite MALI vs SiO_2
324   classification diagram(after [32]),they are magnesian calcic and calc-alkalic granitoids, though
325   one sample are alkali-calcic (Figure 16c, d). These combination patterns are very similar to the
326   typical archean TTG pattern.
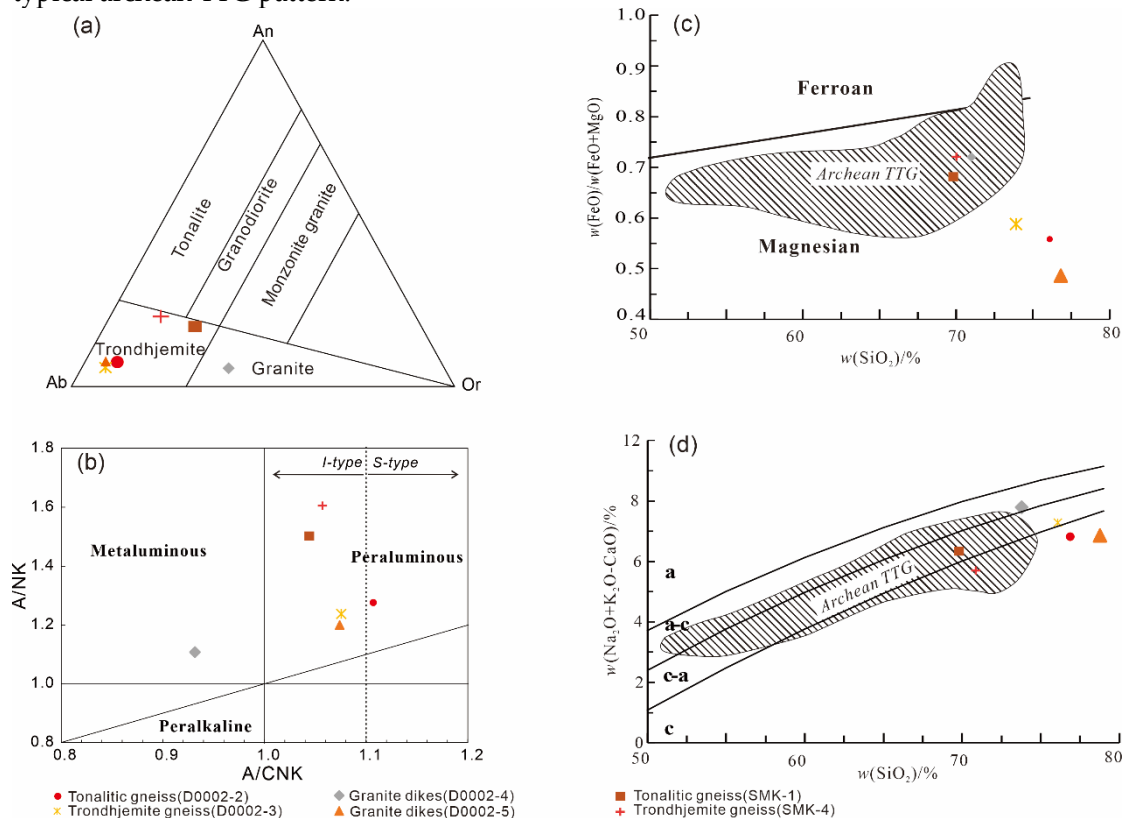
328   **Figure 16.** (a): The TTG suite of rocks plotted on the CIPW an–ab–or classification diagram
329   (after [34]). An = anorthite, Ab = albite, Or = orthoclase;(b)A/NK-A/CNK diagram of granitoids
330   (after [35])；(c) $FeO^t/(FeO^t+MgO)$-SiO_2 classification diagram (after [36]);(d)Granite MALI vs
331   SiO_2 classification diagram(after [36]).a, alkalic; a-c alkali-calcic; c-a calc-alkalic; c,calcic.
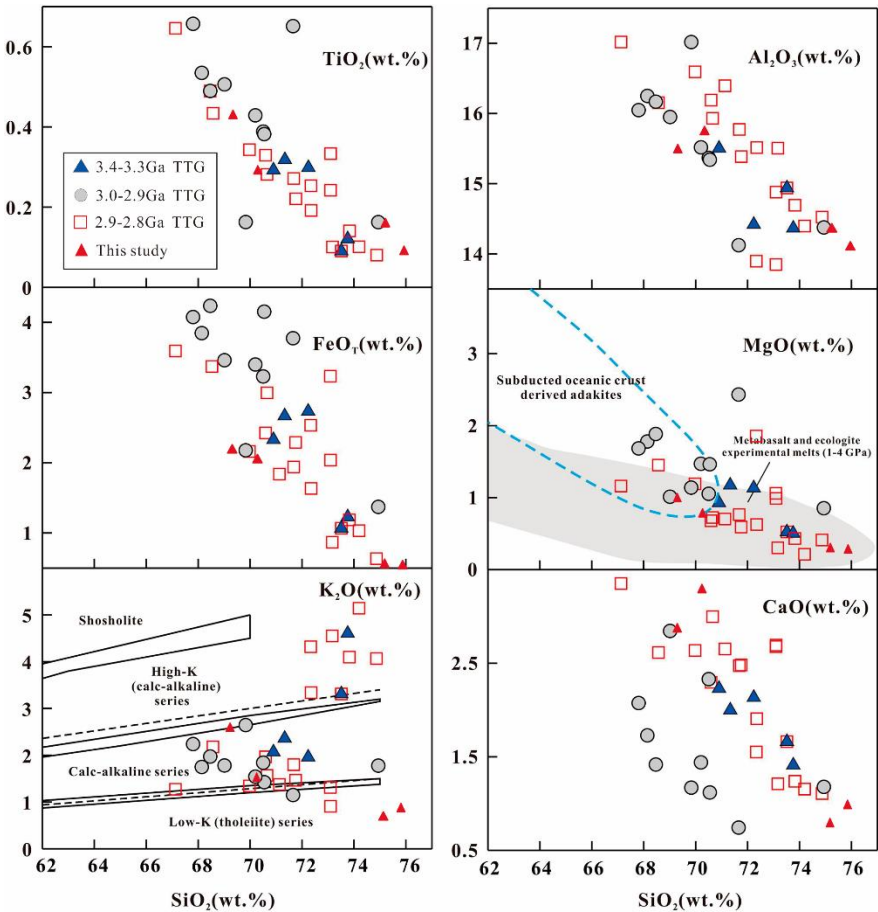
Figure 17. diagrams of gneissic granitoids from the Northern Kongling Terrane, showing SiO2vs. (a) Na2O, (b) K2O, (c) Mg#, (d) MgO, (e) TFe2O3, and (f) CaO. Symbols: diamonds,TTGs; circles, biotite-granites; squares, two-mica granites; triangles, A-type granites. Data sources include this and previous studies ([7, 13, 15, 19, 37-39] and Y.B. Wu's unpublished data).
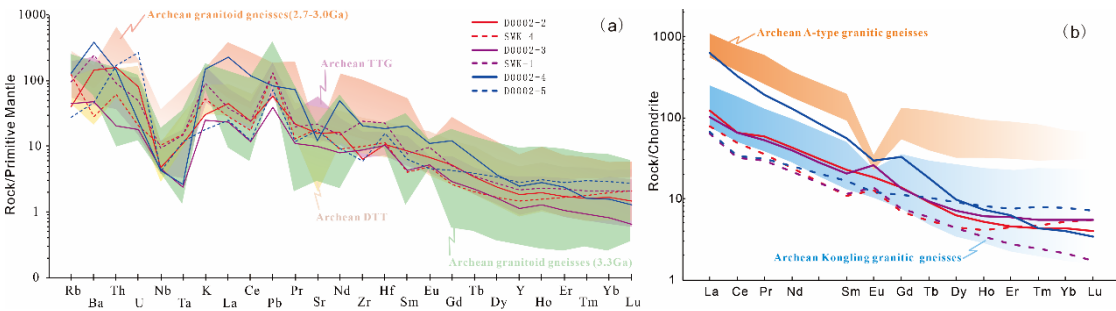
Figure 18. Primitive-mantle-normalized trace element distributions and Chondrite-normalized rare earth element patterns in the Archean TTG and granite dikes from the Kongling Terrane. Normalizing values are from [40]. The red and purple lines are for Kongling TTGs (D0002-2 and SMK-4 for tonalitic gneiss, and D0002-3 and SMK-1 for trondhjemite gneiss), and the blue lines are for granite dikes (D0002-4 and D0002-5). Data for the Archean granitoid gneisses, Archean TTG, and Archean DTT are from Gao et al. [7], Guo et al. [13], and Guo et al.[16], respectively. for the Archean TTG and granite dikes from the Kongling Terrane.
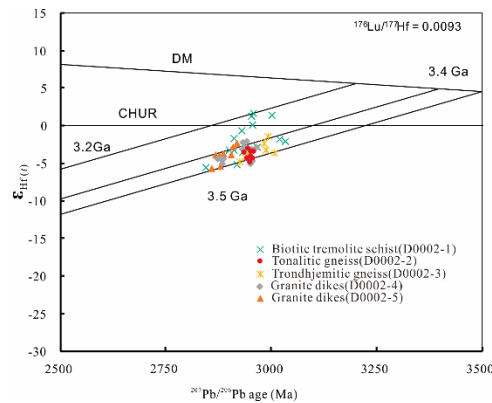
Figure 19. εHf(t) versus $^{207}Pb/^{206}Pb$ zircon age diagram for the biotite–tremolite schists, tonalitic gneisses, trondhjemitic gneisses, and granitic dikes.
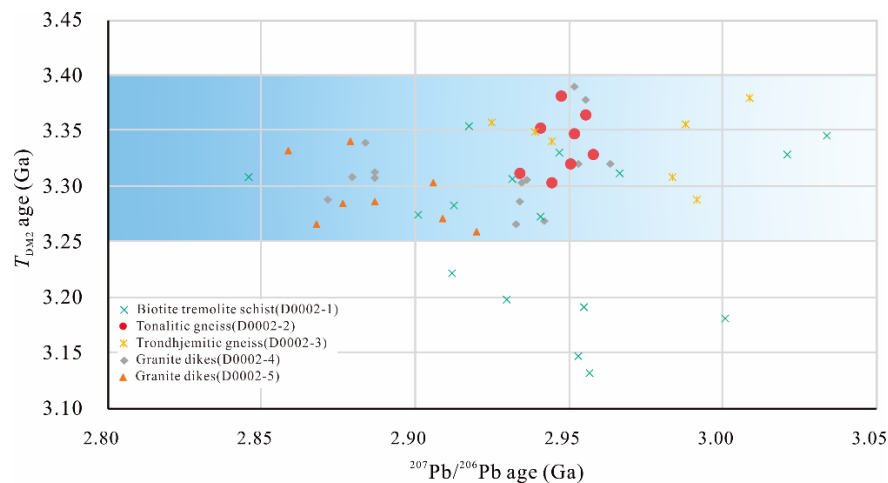
Figure 20. TDM2 age versus $^{207}Pb/^{206}Pb$ zircon age diagram for the biotite–tremolite schists, tonalitic gneisses, trondhjemitic gneisses, and granitic dikes.

Their trace element compositions are characterized by lower total REE values (53.69–105.08 ppm), enrichments in large ion lithophile elements (LILEs), depletions in high field strength elements (HFSEs) (e.g., Ti, Nb, Ta, and P), and low Cr (1.52–6.66 ppm) and Ni (2.87–4.88 ppm) contents (Figure 17a). They show moderate amounts of heavy rare earth elements (HREEs) (e.g., 0.36–0.92 ppm Yb) and depletions in Eu (Eu/Eu*1.00–1.52) (Figure 17b; Table 6). These features make them similar to the rocks of the classic Archean TTG suite in this area [13, 16, 41].

4.2.3. Granite Dikes

The two samples of granite gneisses from the dikes plot in the granite field on a K_2O vs. SiO_2 diagram with relatively high contents of SiO_2 (73.97 and 78.74 wt%), Na_2O (4.41 and 5.98 wt%), K_2O (4.28 and 0.52 wt%), and Al_2O_3 (13.11 and 12.85 wt%), and relatively low values of Mg# (30 and 55). The total contents of REEs are variable (443.68 and 62.35 ppm), but both samples show moderately negative Eu anomalies (Eu/ Eu* = 0.67–0.87; Figure 18b), notable depletions in Sr, P, and Eu, moderate depletions in Nb and Ta, enrichments in HFSEs (Th, U, Zr, and Hf), and alkali granite affinities (Figure 18a).

4.2.4. Zircon Hf-isotope

The zircon Lu–Hf isotopic data are given in Supplementary Data Table S7, and the $^{176}Hf/^{177}Hf(t)$ ratios were calculated back to their measured $^{207}Pb/^{206}Pb$ ages. The εHf values were

370 calculated with reference to a chondritic reservoir (CHUR). The values of $^{176}Lu/^{177}Hf$ and
371 $^{176}Hf/^{177}Hf$ for the CHUR were 0.0336 and 0.282785, respectively [42]. A decay constant of 1.867
372 $\times 10^{-5}$ Ma^{-1} [43] was used for ^{176}Lu. The single-stage model age (T_{DM1}) was calculated relative to
373 depleted mantle with present-day values of 0.28325 for $^{176}Hf/^{177}Hf$ and 0.0384 for $^{176}Lu/^{177}Hf$
374 [30]. The two-stage model age (T_{DM2}), interpreted as the crust formation age, was calculated by
375 projecting the zircon $^{176}Hf/^{177}Hf(t)$ values back to the depleted-mantle model growth curve
376 assuming a $^{176}Lu/^{177}Hf$ ratio of 0.0093 for the upper continental crust [44].

377   The Lu–Hf isotopes of 53 zircons from five samples were analyzed. As illustrated in Table
378 7, the $^{176}Hf/^{177}Hf(t)$ ratios of the concordant zircons show two distinct groups: the biotite–
379 tremolite schists and others. The $^{176}Hf/^{177}Hf(t)$ ratios of the biotite–tremolite schists are higher
380 than the ratios in the TTG gneisses and granitic dikes, ranging from 0.28077 to 0.28094 for the
381 biotite–tremolite schists through 0.28075 to 0.28083 for the TTG gneisses and 0.28075 to 0.28085
382 for the granitic dikes. The εHf(t) values of concordant zircons in the biotite–tremolite schists
383 are close to 0 but range from 1.8 to –5.4 (Figure 19). The concordant zircons of the five samples
384 have T_{DM2} ages ranging from 3.56 to 3.21 Ga (Figure 20).

5. DISCUSSION

5.1. Petrogenesis

5.1.1. Biotite Tremolite-schist

388   Although the Archean TTGs in the Kongling Terrane have been reported on and described
389 by Guo, Gao [13] and [16], there has been relatively little research on Archean metabasites in
390 the Yangtze Craton [45].
391   We noted in section of Whole-rock major and trace element compositions that all our
392 Archean metabasite samples fall into the basaltic andesite and calc-alkaline series in the TAS
393 volcanic rock classification. However, since the mobility of Si, Na, Ca, Rb, K, Sr, Ba, Fe, P, and
394 Pb may have caused changes in the composition of volcanic rocks in Archean greenstone belts
395 [46, 47], we selected instead Zr, Ti, Nb, and Y for classifying these rocks, but a similar result
396 was obtained (Figure 15). We conclude, therefore, that the protoliths of the biotite–tremolite
397 schists were calc-alkaline basaltic andesites, and their high ratios of K_2O/Na_2O (12.8) show that
398 they were high-K island-arc volcanic rocks, and these rocks are generally considered to form
399 by the partial melting of subducted oceanic crust.

5.1.2. TTG Magmatism

401   The ca. 2.9 Ga TTG gneisses are widespread in the North Kongling Terrane [7, 9, 15, 23,
402 39, 48, 49], and these felsic aluminous rocks are characterized by low Y (<18 ppm) and Yb (<1
403 ppm) contents as well as insignificant negative Eu anomalies, consistent with the definition of
404 typical adakitic TTG rocks[50]. Typical suites of TTG and modern adakites were originally
405 considered to result from the partial melting of a young and hot subducted oceanic crust [50,
406 51]. Subsequent studies have shown that such rocks can also be formed by (1) fractional
407 crystallization of mafic minerals (mainly amphibole) in hydrous basaltic magmas under high
408 pressure [52], (2) partial melting of adakitic melt-metasomatized lithospheric mantle [53], (3)
409 partial melting of ancient thickened lower crust [54], (4) partial melting of a delaminated lower
410 continental crust that underwent subsequent interaction with the surrounding asthenosphere
411 [55], or (5) partial melting of pre-existing adakitic or TTG-like (mainly tonalitic) rocks [56].
412   The major element compositions of the TTG samples fall close to the field of partial melts
413 from tonalite and low-K mafic rocks as the 3.3Ga-2.9Ga TTGs [16](Figure 21). They show weak
414 Eu and Sr anomalies, low contents of HREEs (e.g., 0.36–0.92 ppm Yb), and moderate La_N/Yb_N
415 ratios (15–29), indicating an eclogite-facies source region [57](Figure 18). The ca. 2.9 Ga TTG
416 gneisses also exhibit variable values of $Mg^{\#}$ (41–47) and very low contents of Cr (1.7–12.32 ppm)

417   and Ni (2.87–8.41 ppm), therefore, the participation of the mantle source in their genesis is
418   unlikely. Mantle rocks in the subduction zone are enriched during slab melting, that is not
419   consistent with the low contents of trace and rare earth elements in TTG. The geochemistry and
420   Lu–Hf isotope characteristics of the Mesoarchean TTG suggest that their parent melt formation
421   could have been associated with high degrees of melting of the older TTG (tonalite) associations
422   or low-K mafic rocks (**Figure 21**), possibly in a subduction zone [58-60]. Mafic xenoliths or veins
423   hosted in the ca. 2.9 Ga TTGs [39, 45, 61] have chemical affinities to typical island arc basalts,
424   which lends support to an origin in a subduction setting. The possible tectonic settings include
425   an oceanic island arc setting and a continental arc setting[39].

426
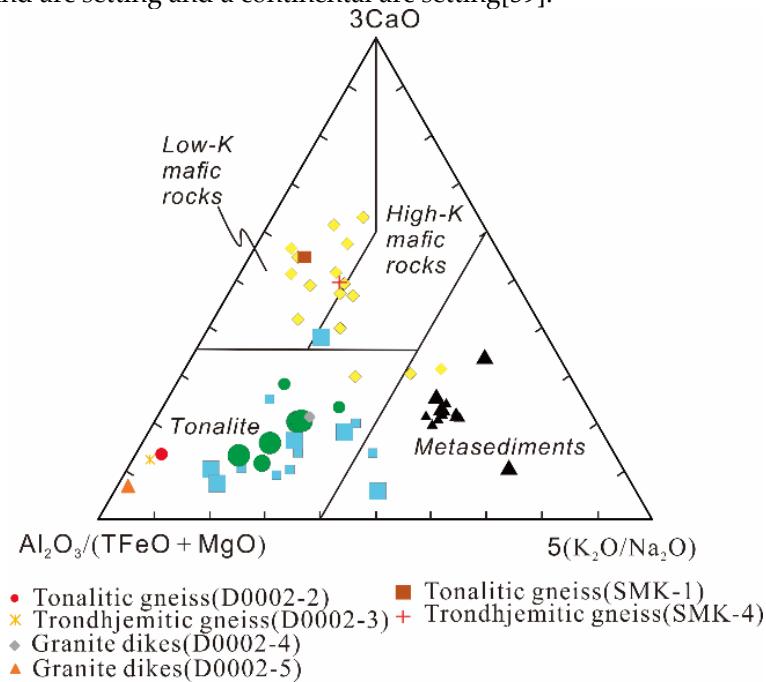
Figure 21. Ternary diagram of Al_2O_3/(TFeO + MgO) vs. 3CaO vs. 5(K_2O/Na_2O) (after Laurent
et al., 2014). The different fields represent the compositions of melts derived from a range of
potential sources (tonalites, metasediments, low- and high-K mafic rocks), determined by the
major-element compositions of partial melts in experimental studies (see references in Laurent
et al., 2014). Symbols: diamonds = TTGs, circles = biotite granites, squares = two-mica granites,
triangles = A-type granites. Data sources include this and previous studies[7, 13, 15, 19, 37-39]
and unpublished data of Wu Y.B..

434   In oceanic island arcs, both the subducting and the overriding plates are juvenile oceanic
435   crust. Thus, the granitoids produced in such an environment would exhibit radiogenic Hf
436   isotopic compositions, with depleted mantle-like εHf(t) values [62]. This conflicts with the non-
437   radiogenic nature of the zircons in the ca. 2.9 Ga TTG rocks, which exhibit a wide range of
438   εHf(t) values, but with predominantly subchondritic values (Figure 19 and Figure 20). The >3.2
439   Ga T_{DM2} ages and the small number of 3.2 Ga inherited zircons in the 3.0–2.9 Ga TTG gneisses
440   [23] indicate a vital role was played by an ancient crystalline basement in the genesis of these
441   rocks, which actually fits a continental arc setting. In continental arcs, due to the melting and/or
442   contamination of the overriding thick ancient continental crust above the subduction zone, the
443   granitoid magmas therein are commonly imprinted by less radiogenic Hf features and
444   characterized by lower εHf(t) values [63-65]. Therefore, the tectonic environment of the
445   Kongling Terrane during the period 3.0–2.9 Ga may have been like a modern continental arc,
446   indicating that plate tectonics in the Yangtze Craton commenced before 2.9 Ga.
447   Fourteen zircons from trondhjemitic gneisses containing core–rim structures yielded an
448   upper intercept age of 3.00 Ga (Figure 18a and Table 6), and they might represent zircons

449   inherited from their parental rocks. The Lu–Hf isotopes also provide the same εHf(t) values
450   and single- and two-stage model ages as the metamorphic zircon cores of the biotite–tremolite
451   schists. All this evidence seems to be generally consistent with the proposal that the TTGs were
452   derived from the partial melting of juvenile crust in the same subduction setting that produced
453   the parental magmas of the metamorphosed basaltic andesite from subducted oceanic crust.
454   These parental magmas might indeed have contributed to the juvenile crust through a process
455   of underplating.

456   *5.2. Tectonic implications*

457   The recently discovered biotite–tremolite schists in the Kongling Terrane, the subject of
458   this paper, are among the oldest rocks of the Yangtze Craton. Consequently, understanding
459   their genesis and evolution is key to understanding the initiation of plate tectonics in South
460   China.

461   Two groups of zircon $^{206}Pb/^{207}Pb$ ages were obtained from the zircons with core–rim
462   structures of the biotite–tremolite schists, with the cores giving the older age of 3.00 Ga.
463   Although the Th/U ratios in the cores are slightly higher than in the rims, their images are light-
464   colored with flower shapes or cloud rings, which are characteristics of recrystallized zircons
465   (Figure 4). The 3.00 Ga ages of the zircon cores can probably be treated as a record of early
466   metamorphic/magmatic events. The low contents of U in the zircons might result in the
467   metamorphic ages still falling on or near the concordant curve.

468   The Lu–Hf isotope data also indicate that the biotite–tremolite schists formed at around
469   3.00 Ga, which is the same age as shown by the metamorphic zircon cores. The single- and two-
470   stage model ages of hafnium are 3.26 Ga and 3.39 Ga, respectively, and these ages are within
471   error of the ages of the metamorphic zircon cores. These very close age data combined with the
472   geochemical character of high-K island-arc volcanic rocks (in 5.1.1) suggest the protolith of the
473   metamorphosed basaltic andesites were derived from the partial melting of juvenile crust in a
474   subduction zone setting

475   Apart from the magmatic events, ages of 2.93 Ga were obtained from both cores and rims.
476   These 2.93 Ga zircons cores show dark CL images and low Th/U ratios (<0.1), indicating that
477   the grains underwent a metamorphic recrystallization in the presence of fluids. The rims of the
478   zircons show uniform structures in the CL images, and they have low Th/U ratios (<0.1). As the
479   zircons with higher U contents display greater Pb loss, the data from the analytical spots fall
480   on the discordia curve with a 2.93 Ga upper intercept age. These two important thermal events
481   can also be observed in the age data for the zircons from the Dongchonghe TTG rocks (D0002-
482   2 and D0002-3), which are interpreted to be the same as other tectonothermal events recorded
483   by zircons, as described by Gao et al.[7], Qiu et al.[9], and Zhang et al. [10].

484   The 3.3–3.0 Ga metamorphic/magmatic events might be related to the subduction of
485   oceanic crust that produced the trondhjemites and the high-K calc-alkaline island-arc basaltic
486   andesites. The 2.93–2.91 Ga ages would be related to the first metamorphic event that occurred
487   when the TTG granites and tholeiitic basaltic rock enclaves were transformed into TTG gneisses
488   and amphibolite enclaves, respectively, while the ~2.87 Ga alkaline magmatism was related to
489   a regional post-orogenic extensional environment. Guo, Wu [16] pointed out that the granitoid
490   magmatism changed from TTG- to granite-dominated after 2.8 Ga, and this change may reflect
491   a transition from subduction to collision-related events.

492   Taking into account the several tectonic/magmatic thermal events that have been
493   described in the previous literature at 2.75–2.70 Ga and 2.6–2.5 Ga [61], and 2.1–1.9 Ga [12, 17,
494   66-68], our latest data show that the Yangtze continental nucleus underwent at least five
495   widespread tectonic/magmatic thermal events during the Paleoproterozoic and the
496   Mesoarchean.

497   **6. CONCLUSIONS**

498   1) The ages of the early cores of zircons from the biotite–tremolite schist enclaves hosted
499   by the TTG gneisses in the Kongling high-grade metamorphic terrane of the Yangtze Craton,
500   China, are similar to the metamorphic recrystallization ages and model ages indicated by
501   Hafnium isotopes (ca. 3.00 Ga), which suggests that the basaltic protoliths of these schists were
502   formed before or close to 3.00 Ga. The data indicate that these schists represent the
503   metamorphosed basaltic igneous rocks that formed the basal part of a Mesoarchean granite–
504   greenstone belt.

505   2) The host TTG gneisses were derived from the partial melting of subducted oceanic crust,
506   which is consistent with the proposal that the early metamorphic/tectonic thermal events in the
507   Yangtze continental core record the initiation of global plate tectonics at 3.00 Ga.

508   **Author Contributions:** Conceptualization, Wenxiao Zhou and Yunxu Wei; Data curation, Wenxiao Zhou,
509   Yunxu Wei and Haiquan Li; Formal analysis, Wenxiao Zhou; Project administration, Yunxu Wei;
510   Resources, Zhengxiang Hu, Xianxiao Huang and Xiaoming Zhao; Writing – original draft, Wenxiao Zhou;
511   Writing – review & editing, Wenxiao Zhou.

512   **Funding:** This study is supported by the National Natural Science Foundation of China (No. 41703024)
513   and the work items of China Geological Survey (No. DD20190374, DD20160029, 12120113061700).

514   **Conflicts of Interest:** The authors declare no conflict of interest.

References

515 **References**

516   1.   Hacker, B.R., et al., *U/Pb zircon ages constrain the architecture of the ultrahigh-pressure Qinling–*
517   *Dabie Orogen, China.* Earth and Planetary Science Letters, 1998. **161**(1): p. 215-230.

518   2.   Li, S., et al., *Collision of the North China and Yangtse Blocks and formation of coesite-bearing*
519   *eclogites: Timing and processes ☆.* Chemical Geology, 1993. **109**(1-4): p. 89-111.

520   3.   Zhang, S.-B. and Y.-F. Zheng, *Formation and evolution of Precambrian continental lithosphere in*
521   *South China.* Gondwana Research, 2013. **23**(4): p. 1241-1260.

522   4.   Wu, Y.B., et al., *Zircon U-Pb age and trace element evidence for Paleoproterozoic granulite-facies*
523   *metamorphism and Archean crustal rocks in the Dabie Orogen.* Lithos, 2008. **101**(3-4): p. 308-
524   322.

525   5.   Wu, F.-Y., et al., *Zircon U–Pb and Hf isotopic constraints on the Early Archean crustal evolution in*
526   *Anshan of the North China Craton.* Precambrian Research, 2008. **167**(3-4): p. 339-362.

527   6.   Song, B., et al., *3800 to 2500 Ma crustal evolution in the Anshan area of Liaoning Province,*
528   *northeastern China.* Precambrian Research, 1996. **78**(79): p. 79-94.

529   7.   Gao, S., et al., *Age and growth of the Archean Kongling terrain, South China, with emphasis on 3.3*
530   *Ga granitoid gneisses.* Geochimica Et Cosmochimica Acta Supplement, 2011. **72**(12): p. 153-182.

531   8.   Jiao, W.F., et al., *The oldest basement rock in the Yangtze Craton revealed by zircon U-Pb age and*
532   *Hf isotope composition.* Science In China Series D-Earth Sciences, 2009. **52**(9): p. 1393-1399.

533   9.   Qiu, Y., et al., *First evidence of >3.2 Ga continental crust in the Yangtze craton of south China and*
534   *its implications for Archean crustal evolution and Phanerozoic tectonics.* Geology, 2000. **28**(1): p.
535   11.

536   10. Zhang, S.B., et al., *Zircon U-Pb age and Hf isotope evidence for 3.8 Ga crustal remnant and*
537   *episodic reworking of Archean crust in South China.* Earth And Planetary Science Letters, 2006.
538   **252**(1-2): p. 56-71.

539   11. Qiu, X.-F., et al., *Evolution of the Archean continental crust in the nucleus of the Yangtze block:*
540   *Evidence from geochemistry of 3.0 Ga TTG gneisses in the Kongling high-grade metamorphic*
541   *terrane, South China.* Journal of Asian Earth Sciences, 2018. **154**: p. 149-161.

542   12. Ling, W., et al., *Sm-Nd isotope geochronology of the Qiling complex in the Huangling area of the*
543   *Yangtze Craton.* Chinese Science Bulletin, 1998. **43**(1): p. 86.

544   13. Guo, J.L., et al., *3.45 Ga granitic gneisses from the Yangtze Craton, South China: Implications for*
545   *Early Archean crustal growth.* Precambrian Research, 2014. **242**: p. 82-95.

546   14. Liu, X., et al., *Precambrian crustal growth of Yangtze Craton as revealed by detrital zircon studies.*
547   American Journal of Science, 2008. **308**(4): p. 421-468.

548   15. Chen, K., et al., *2.6-2.7 Ga crustal growth in Yangtze craton, South China.* Precambrian Research,
549   2013. **224**: p. 472-490.

550   16. Guo, J.L., et al., *Episodic Paleoarchean-Paleoproterozoic (3.3-2.0 Ga) granitoid magmatism in*
551   *Yangtze Craton, South China: Implications for late Archean tectonics.* Precambrian Research, 2015.
552   **270**: p. 246-266.

553   17. Zhang, S.B., et al., *Zircon U-Pb age and Hf-O isotope evidence for Paleoproterozoic metamorphic*
554   *event in South China.* Precambrian Research, 2006. **151**(3): p. 265-288.

555   18. Li, Z., et al., *Grenvillian continental collision in south China: New SHRIMP U-Pb zircon results and*
556   *implications for the configuration of Rodinia.* Geology, 2002. **30**(2): p. 163-166.

557   19.   Gao, S., et al., *Contrasting geochemical and Sm-Nd isotopic compositions of Archean*
558   *metasediments from the Kongling high-grade terrain of the Yangtze craton: Evidence for cratonic*
559   *evolution and redistribution of REE during crustal anatexis.* Geochimica Et Cosmochimica Acta,
560   1999. **63**(13-14): p. 2071-2088.

561   20.   Ling, W., et al., *Neoproterozoic magmatic events within the Yangtze continental interior and along*
562   *its northern margin and their tectonic implication: constraint from the ELA-ICPMS U-Pb*
563   *geochronogy of zicrons from the Huangling and Hannan complexes*, in *Acta Petrologica Sinica*.
564   2006. p. 387-396.

565   21.   Wei, Y., et al., *SHRIMP zircon U-Pb ages and geochemical characteristics of the neoproterozoic*
566   *granitoids in the Huangling anticline and its tectonic setting.* Journal of Earth Science, 2012. **23**(5):
567   p. 659-676.

568   22.   Zhang, S.-B., et al., *Neoproterozoic anatexis of Archean lithosphere: Geochemical evidence from*
569   *felsic to mafic intrusions at Xiaofeng in the Yangtze Gorge, South China.* Precambrian Research,
570   2008. **163**(3-4): p. 210-238.

571   23.   Zhang, S.B., et al., *Zircon isotope evidence for ⩾3.5Ga continental crust in the Yangtze craton of*
572   *China.* Precambrian Research, 2006. **146**(1): p. 16-34.

573   24.   Ballard, J.R., et al., *Two ages of porphyry intrusion resolved for the super-giant Chuquicamata*
574   *copper deposit of northern Chile by ELA-ICP-MS and SHRIMP.* Geology, 2001. **29**(5): p. 383-386.

575   25.   Yuan, H., et al., *Accurate U-Pb age and trace element determinations of zircon by laser ablation-*
576   *inductively coupled plasma-mass spectrometry.* Geostandards and Geoanalytical Research, 2004.
577   **28**(3): p. 353-370.

578   26.   Andersen, T., *Correction of common lead in U–Pb analyses that do not report 204Pb.* Chemical
579   geology, 2002. **192**(1-2): p. 59-79.

580   27.   Ludwig, K.R., *Isoplot 3.00: A geochronological toolkit for Microsoft Excel.* Berkeley Geochronology
581   Center Special Publication, 2003. **4**: p. 70.

582   28.   Hu, Z., et al., *Improved in situ Hf isotope ratio analysis of zircon using newly designed X skimmer*
583   *cone and jet sample cone in combination with the addition of nitrogen by laser ablation multiple*
584   *collector ICP-MS.* Journal of Analytical Atomic Spectrometry, 2012. **27**(9): p. 1391-1399.

585   29.   Hu, Z., et al., *A "wire" signal smoothing device for laser ablation inductively coupled plasma mass*
586   *spectrometry analysis.* Spectrochimica Acta Part B: Atomic Spectroscopy, 2012. **78**: p. 50-57.

587   30.   Griffin, W.L., et al., *Zircon chemistry and magma mixing, SE China: in-situ analysis of Hf isotopes,*
588   *Tonglu and Pingtan igneous complexes.* Lithos, 2002. **61**(3-4): p. 237-269.

589   31.   Winchester, J.A. and P.A. Floyd, *Geochemical discrimination of different magma series and their*
590   *differentiation products using immobile elements.* Chemical Geology, 1977. **20**: p. 325-343.

591   32.   Pearce, J.A., *A user's guide to basalt discrimination diagrams.* Trace element geochemistry of
592   volcanic rocks: applications for massive sulphide exploration. . Vol. 12. 1996: Geological Association
593   of Canada, Short Course Notes. 79-113.

594   33.   Miyashiro, A., *Volcanic rock series in island arcs and active continental margins.* American journal
595   of science, 1974. **274**(4): p. 321-355.

596   34.   O'connor, J., *A classification for quartz-rich igneous rocks based on feldspar ratios.* US Geological
597   Survey Professional Paper B, 1965. **525**: p. 79-84.

598   35.   Maniar, P.D. and P.M. Piccoli, *Tectonic discrimination of granitoids.* Geological society of America
599   bulletin, 1989. **101**(5): p. 635-643.

600 36. Frost, B.R., et al., *A geochemical classification for granitic rocks.* Journal of petrology, 2001. **42**(11):
601   p. 2033-2048.

602 37. Peng, M., et al., *Geochemistry, zircon U–Pb age and Hf isotope compositions of Paleoproterozoic*
603   *aluminous A-type granites from the Kongling terrain, Yangtze Block: Constraints on petrogenesis*
604   *and geologic implications.* Gondwana Research, 2012. **22**(1): p. 140-151.

605 38. Xiong, Q., et al., *Zircon U-Pb age and Hf isotope of Quanyishang A-type granite in Yichang:*
606   *signification for the Yangtze continental cratonization in Paleoproterozoic.* Chinese Science
607   Bulletin, 2009. **54**(3): p. 436-446.

608 39. Li, L., et al., *Geochronology and geochemistry of igneous rocks from the Kongling terrane:*
609   *Implications for Mesoarchean to Paleoproterozoic crustal evolution of the Yangtze Block.*
610   Precambrian Research, 2014. **255**: p. 30-47.

611 40. Sun, S.S. and W.F. McDonough, *Chemical and isotopic systematic of Oceanic basalt: Implications*
612   *for the mantal composition and processes.* Vol. 42. 1989, Geological Society, London, Special
613   Publications. 313-345.

614 41. Gao, S. and B.R. Zhang, *Discovery of the Archean TTG gneiss in the northern part of the Yangtze*
615   *platform and its significance.* Earth Science-Journal of China University of Geosciences, 1990. **15**(6):
616   p. 675-679.

617 42. Bouvier, A., J.D. Vervoort, and P.J. Patchett, *The Lu–Hf and Sm–Nd isotopic composition of CHUR:*
618   *constraints from unequilibrated chondrites and implications for the bulk composition of terrestrial*
619   *planets.* Earth and Planetary Science Letters, 2008. **273**(1-2): p. 48-57.

620 43. Söderlund, U., et al., *The 176Lu decay constant determined by Lu–Hf and U–Pb isotope systematics*
621   *of Precambrian mafic intrusions.* Earth and Planetary Science Letters, 2004. **219**(3-4): p. 311-324.

622 44. Vervoort, J.D. and P.J. Patchett, *Behavior of hafnium and neodymium isotopes in the crust:*
623   *constraints from Precambrian crustally derived granites.* Geochimica et Cosmochimica Acta, 1996.
624   **60**(19): p. 3717-3733.

625 45. Wei, J.Q. and M.M. Jing, *Chronology and geochemistry of amphibolites from the Kongling complex.*
626   Chinese Journal of Geology, 2013. **48**(4): p. 970-983.

627 46. Polat, A. and A. Hofmann, *Alteration and geochemical patterns in the 3.7–3.8 Ga Isua greenstone*
628   *belt, West Greenland.* Precambrian Research, 2003. **126**(3-4): p. 197-218.

629 47. Polat, A., A. Hofmann, and M.T. Rosing, *Boninite-like volcanic rocks in the 3.7–3.8 Ga Isua*
630   *greenstone belt, West Greenland: geochemical evidence for intra-oceanic subduction zone*
631   *processes in the early Earth.* Chemical geology, 2002. **184**(3-4): p. 231-254.

632 48. Guo, J.-L., et al., *Episodic Paleoarchean-Paleoproterozoic (3.3–2.0 Ga) granitoid magmatism in*
633   *Yangtze Craton, South China: Implications for late Archean tectonics.* Precambrian Research, 2015.
634   **270**: p. 246-266.

635 49. Zheng, J., et al., *Widespread Archean basement beneath the Yangtze craton.* Geology, 2006. **34**(6):
636   p. 417-420.

637 50. Defant, M.J. and M.S. Drummond, *Derivation of some modern arc magmas by melting of young*
638   *subducted lithosphere.* Nature, 1990. **347**(6294): p. 662.

639 51. Barker, F. and J.G. Arth, *Generation of trondhjemitic-tonalitic liquids and Archean bimodal*
640   *trondhjemite-basalt suites.* Geology, 1976. **4**(10): p. 596-600.

641 52. Castillo, P.R., *An overview of adakite petrogenesis.* Chinese science bulletin, 2006. **51**(3): p. 257-
642   268.

643   53.   Gao, Y., et al., *Adakitic rocks from slab melt-modified mantle sources in the continental collision*
644   *zone of southern Tibet.* Lithos, 2010. **119**(3-4): p. 651-663.
645   54.   Chung, S.-L., et al., *Adakites from continental collision zones: melting of thickened lower crust*
646   *beneath southern Tibet.* Geology, 2003. **31**(11): p. 1021-1024.
647   55.   Gao, S., et al., *Recycling lower continental crust in the North China craton.* Nature, 2004. **432**(7019):
648   p. 892-7.
649   56.   Moyen, J.-F., *High Sr/Y and La/Yb ratios: the meaning of the "adakitic signature".* Lithos, 2009.
650   **112**(3-4): p. 556-574.
651   57.   Moyen, J.-F., *The composite Archaean grey gneisses: petrological significance, and evidence for a*
652   *non-unique tectonic setting for Archaean crustal growth.* Lithos, 2011. **123**(1-4): p. 21-36.
653   58.   Martin, H. and J.-F. Moyen, *Secular changes in tonalite-trondhjemite-granodiorite composition as*
654   *markers of the progressive cooling of Earth.* Geology, 2002. **30**(4): p. 319-322.
655   59.   Martin, H., et al., *An overview of adakite, tonalite–trondhjemite–granodiorite (TTG), and sanukitoid:*
656   *relationships and some implications for crustal evolution.* Lithos, 2005. **79**(1-2): p. 1-24.
657   60.   Moyen, J.-F. and H. Martin, *Forty years of TTG research.* Lithos, 2012. **148**: p. 312-336.
658   61.   Wei, J. and J. Wang, *Zircon age and Hf isotope compositions of amphibolite enclaves from the*
659   *Kongling complex.* Geol. J. China Univ., 2012. **18**(4): p. 589-600.
660   62.   Schaltegger, U., et al., *Multiple mantle sources during island arc magmatism: U–Pb and Hf isotopic*
661   *evidence from the Kohistan arc complex, Pakistan.* Terra Nova, 2002. **14**(6): p. 461-468.
662   63.   Ducea, M.N., J.B. Saleeby, and G. Bergantz, *The Architecture, Chemistry, and Evolution of*
663   *Continental Magmatic Arcs.* Annual Review of Earth and Planetary Sciences, 2015. **43**(1): p. 299-
664   331.
665   64.   Jones, R.E., et al., *Geodynamic controls on the contamination of Cenozoic arc magmas in the*
666   *southern Central Andes: Insights from the O and Hf isotopic composition of zircon.* Geochimica et
667   Cosmochimica Acta, 2015. **164**: p. 386-402.
668   65.   Li, Z.-X., et al., *Magmatic switch-on and switch-off along the South China continental margin since*
669   *the Permian: Transition from an Andean-type to a Western Pacific-type plate boundary.* 2012. **532**:
670   p. 271-290.
671   66.   Han, Q.S., et al., *A ca.2.1 Ga Andean-type margin built on metasomatized lithosphere in the*
672   *northern Yangtze craton, China: Evidence from high-Mg basalts and andesites.* Precambrian
673   Research, 2017. **309**: p. 309-324.
674   67.   Ling, W.L. and S. Gao, *The tectonic thermal events and the evolution in the late Paleoproterozoic*
675   *of the Yangtze craton in the Yangtze.* Chinese Science Bulletin, 2000. **45**(21): p. 2343-2347.
676   68.   Peng, S., et al., *The discovery of Paleoproterozoic ophiolitic melange   in the northern part of the*
677   *Huangling Dome of the Yangtze Craton.* Journal of Earth Science, 2016. **41**(12): p. 2117-2118.
678